JOURNAL OF GEOPHYSICAL RESEARCH, VOL. 95, NO. C6, PAGES 9701-9711, JUNE 15, 1990

Estimating and Removing Sensor-Induced Correlation From Advanced Very High Resolution Radiometer Satellite Data

LAURENCE C. BREAKER

NOAA/NWS, National Meteorological Center, Camp Springs, Maryland

In order to estimate the spatial covariance structure of sea surface temperature (SST) using advanced very high resolution radiometer (AVHRR) satellite data, autocorrelation induced by the sensor itself must be determined and then removed before the correlative properties of SST per se can be found. Sensor-induced autocorrelation arises from (1) partially redundant sampling and (2) a nonideal impulse response. Simulation techniques are used to model the correlation structure produced by the AVHRR. Results indicate that an autocorrelation of 0.39 at lag 1 arises from the overlap of adjacent pixels in the alongscan direction. Autocorrelations of 0.51 (alongscan) and 0.43 (alongtrack) arise from the sensor impulse response at lag 1. The autocorrelation at lag 2 is still significant (0.07) due to the sensor impulse response in the alongscan direction. Overall, an autocorrelation of 0.46 occurs at lag 1 due to the combined effects of pixel overlap and the sensor impulse response, at nadir. Procedures for removing this sensor-induced correlation are presented. Oceanographically, these results indicate, for example, that the gradients associated with sharp oceanic fronts will be suppressed. Application of the results to observed AVHRR satellite data indicate that correlation length scales for SST over one portion of the Gulf Stream are on the order of 20 km. The results also indicate that the effective spatial resolution of the AVHRR is roughly 1.25 km at nadir, somewhat lower than the commonly accepted value. Finally, it is concluded that the accuracy of the calculations is limited by (1) an incomplete specification of the AVHRR system modulation transfer function (MTF) and (2) the sine wave response function that is used to approximate the system MTF.

INTRODUCTION

In order to determine the spatial correlation structure of sea surface temperature (SST) from advanced very high resolution radiometer (AVHRR) satellite data, it is necessary to consider what influence the AVHRR sensor itself may impose on this structure. Because the AVHRR is a scanning radiometer and because of the method of sampling employed by this instrument, it is possible that the radiances from adjacent picture elements (pixels) do not represent completely independent estimates of SST. Hence we are motivated to examine those characteristics of the AVHRR that may affect the correlative properties, in our case, of SST.

Several recent studies have considered autocorrelation in multispectral scanner (MSS) and thematic mapper (TM) data from the Landsat polar-orbiting satellite [e.g., *Tubbs and Coberly*, 1978; *Craig*, 1979; 1981, 1984*a*; *Craig and Labovitz*, 1980]. The MSS and TM, like the AVHRR, are scanning radiometers. *Tubbs and Coberly* [1978] indicated that due to the physical properties of both the sensor and the target scene, Landsat data are highly correlated. *Craig* [1979] found that Landsat data are highly autocorrelated. To correct for this interdependence between samples, he recommended subsampling the data every tenth pixel. In a subsequent study, *Craig and Labovitz* [1980] suggested that a number of sources may contribute to autocorrelation in Landsat (MSS) data. These sources generally fell into two categories: those related to hardware effects and those arising from natural conditions such as cloud cover, location, and time of year. *Craig* [1982] concluded that the Earth's terrain contributed significantly to the observed autocorrelation in Landsat data. Finally, *Craig* [1984] again identified the importance of terrain in contributing to autocorrelation in Landsat data. He further suggested methods for removing the effects of autocorrelation in these data. It is important to note in these studies that no attempt was made to estimate or separate the effects of possible sensor-induced (auto)correlation from the autocorrelation naturally arising in the remotely sensed fields themselves. Also (to my knowledge), no similar studies have, as yet, been conducted for the AVHRR.

In the following, a brief introduction to the theory of linear systems, a discussion of the AVHRR sensor per se, and calculations of the line spread functions (LSFs) are first presented. Sections follow on simulations of sensor-induced correlation, combining the results, and application to observed data. Finally, there is a discussion section followed by conclusions.

Paper number 90JC00069.

LINEAR SYSTEMS

Any image-forming system may be treated as a black box, if an input signal is operated on to produce an output signal [*Gaskill*, 1978]. For most present generation spaceborne radiometers, the input consists of scene radiances and the output, a corresponding digital signal suitable for transmission to Earth (Figure 1). As indicated, such radiometers may be viewed as being composed of three subsystems, optics at the front end, followed by a detector, and electronics. The following discussion is valid to the extent that radiometers such as the AVHRR can be treated as constant-parameter linear systems [e.g., *Gaskill*, 1978].

In the time domain, if the input to a linear system is $s_i(t)$, then the output from that system, $s_o(t)$, can be determined according to

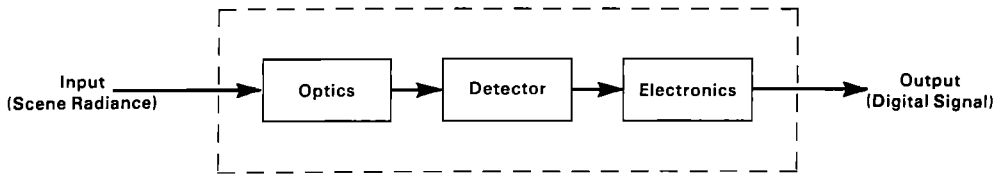

Fig. 1. Schematic diagram of a typical spaceborne radiometer depicting the basic functions that occur from the input scene radiance to the digital signal at the output.

$$s_o(t) = \int_0^\infty h(\tau)s_i(t-\tau)\,d\tau \tag{1}$$

for continuous functions of time. The weight function, $h(\tau)$, is often referred to as the impulse response function. In the frequency domain, (1) can be converted via Fourier transformation to

$$S_o(f) = H(f)S_i(f) \tag{2}$$

where $S_i(f)$ is the Fourier transform of the input, $s_i(t)$, at frequency f, $S_o(f)$ is the Fourier transform of the output, $s_o(t)$, and $H(f)$ is the Fourier transform of $h(\tau)$ and is called the frequency response function or transfer function. The frequency response function of a linear system is generally complex,

$$H(f) = |H(f)|e^{i\phi(f)} \tag{3}$$

where $H(f)$ represents the system gain, $\phi(f)$ the phase shift imposed by the system, and $i = \sqrt{-1}$.

For optical systems, the impulse response function is replaced by the point spread function, PSF(x, y), where time is replaced by x and y, variables which represent orthogonal coordinates in the image domain. The PSF describes the two-dimensional spatial output for a point source. Because actual systems have a nonideal PSF, scene radiance modulation is reduced through the imaging process, resulting in an overall smoothing of the input scene. In an optical system, the output resulting from an arbitrary input spatial pattern can be found through a two-dimensional convolution with the PSF.

Alternatively, the output of an optical system can be expressed in terms of spatial frequency as

$$G_o(\nu_x, \nu_y) = \text{OTF}(\nu_x, \nu_y)G_i(\nu_x, \nu_y) \tag{4}$$

where $\nu_x(\nu_y)$ represents spatial frequency in the $x(y)$ direction and $G_i(\nu_x, \nu_y)$ is the two-dimensional spatial spectrum of the input scene. The OTF(ν_x, ν_y), the optical transfer function, is the Fourier transform of the PSF, and $G_o(\nu_x, \nu_y)$ is the two-dimensional spatial spectrum of the output image. The OTF provides a measure of an imaging system's ability to recreate the spatial frequency content of a scene. Like the frequency response function, the OTF is generally a complex quantity where

$$\text{OTF}(\nu) = \text{MTF}(\nu)e^{i\phi(\nu)} \tag{5}$$

The modulus of the OTF, or modulation transfer function (MTF), represents the system's sine wave amplitude response, and $\phi(\nu)$ indicates the spatial frequency phase shift introduced by the system. For optical systems where the PSF is symmetric, no phase shift occurs, and the OTF is real and identical with the MTF. As pointed out by *Lloyd* [1975], however, thermal imaging systems may differ from other optical and electro-optical devices in several ways, making the OTF construct, in the case of thermal sensors, less than ideal.

In practice, it is not usually possible to measure the two-dimensional PSF directly. Consequently, one-dimensional versions of the PSF in satellite alongscan (x) and alongtrack (y) coordinates are measured independently and the results combined to produce the PSF [*Markham*, 1985]. These one-dimensional versions of the PSF are called line spread functions (LSFs). These functions represent the response of an optical system to an infinitesimally narrow line source, aligned in the appropriate direction. However, to determine the PSF using this approach, it is assumed that the PSF is separable with respect to a rectangular coordinate system. A function of two independent variables is separable with respect to a particular set of coordinates if it can be expressed as a product of two functions, each of which depends on only one independent variable [*Goodman*, 1968]. Thus, if the PSF(x, y) can be expressed as

$$\text{PSF}(x, y) = \text{LSF}_1(x)\text{LSF}_2(y) \tag{6}$$

where $\text{LSF}_1(x)$ and $\text{LSF}_2(y)$ are the corresponding line spread functions in the x and y directions, respectively, then the PSF(x, y) is a separable function. Also, this property of separability allows cumbersome two-dimensional Fourier transforms to be expressed as the product of two simpler one-dimensional Fourier transforms.

THE AVHRR

The AVHRR is an optical-mechanical device consisting of five modules: a scanner, an optical subsystem, a radiant cooler, an electronics module, and a baseplate unit [*ITT-Aerospace*, 1976].

A continuously rotating mirror, rotating at 360 rpm, provides scanning in the alongscan direction. This rate of alongscan scanning is synchronized with the forward motion of the spacecraft to produce quasi-contiguous scan lines of Earth-sensed radiances. The optical subsystem consists of an afocal Cassegrain telescope which collects and collimates the incoming radiation, followed by secondary optics which reimage and separate the incoming radiation into discrete spectral bands and focuses it onto field stops, where it is subsequently detected. The spectral bands for the currently operational four-channel instrument (NOAA 10) are given in Table 1.

Bands 3 and 4 in the IR are separated by a dichroic beam splitter before they are detected. Spectral radiance in band 4 is sensed by a mercury-cadmium-telluride detector, which is

TABLE 1. Wavelength Regions (i.e., Spectral Bands) Utilized by the AVHRR

Band	Wavelength Region, μm
1	0.55–0.68
2	0.725–1.10
3	3.55–3.93
4	10.5–11.5

Starting with NOAA 7 and up through NOAA 11 (the next satellite to be launched in the NOAA series) the odd-numbered satellites carry five-channel instruments. The fifth channel extends from 11.5 to 12.5 μm, and channel four is shifted to 10.3–11.3 μm.

located in the radiant cooler module. The radiant cooler thermally isolates the IR detectors from the optics and maintains them at a temperature of 105 K. The instantaneous field-of-view (IFOV) of the instrument is 1.3×10^{-3} radians in all channels, yielding a nominal spatial resolution at nadir of about 1.08 km at a spacecraft altitude of 833 km, and about 1.13 km at a spacecraft altitude of 870 km.

The electronics module processes the detector outputs to produce digital data suitable for transmission to Earth (or for storage aboard the spacecraft). To accomplish these objectives, the detector outputs are amplified, multiplexed, converted from analog to digital form, and finally sampled at a rate of 40 kHz by the satellite processor to produce digital data with 10-bit resolution. The instrument base plate is the mounting structure to which all the other modules are affixed.

The schematic diagram shown in Figure 1 can be applied to the AVHRR, based on the primary functions performed by the various components which make up the instrument. This simplified functional structure provides a convenient framework for analyzing the behavior of this device.

AVHRR data are sampled at a rate of 1.4 samples per IFOV [*Schwalb*, 1978]. This sampling rate yields adjacent IFOVs which overlap by approximately 40% in the alongscan direction. Although oblique viewing and Earth curvature for increasing scan angles cause distention of the individual pixels, the percent of overlap between adjacent pixels in the alongscan direction remains essentially constant (Figure 2).

In the alongtrack direction, pixel size (i.e., the minor axis of the scan spot ellipse or alongtrack pixel diameter (Figure 2)) also increases with increasing slant range or scan angle. This occurs because the alongtrack ground coverage corresponding to the distance subtended by one IFOV increases with increasing slant range between the satellite and the target (i.e., through similar triangles). This increase in alongtrack pixel diameter versus nadir angle can be expressed approximately as [*Richards*, 1986]

$$b_H = b_0 \sec \theta \tag{7}$$

where b_H is the alongtrack pixel diameter at nadir angle θ and b_0 is the alongtrack pixel diameter at $\theta = 0°$.

This increase in alongtrack pixel diameter leads to increasing overlap between adjacent pixels in the alongscan direction as the slant range increases (Figure 2). For example, at a nadir angle of about 43°, the percent of overlap is approximately 40%. Thus pixel overlap, although arising from different mechanisms, occurs in both the alongscan and alongtrack directions.

MTF data for the AVHRR are provided by the manufacturer at a limited number of spatial frequencies. This system MTF includes the optics, the detector, and the electronics (Figure 1). Alongscan and alongtrack MTF data for band 4 for the AVHRR aboard NOAA 10 are shown in Figure 3. MTF data for frequencies greater than about 0.45 cycles/km are not available, and thus the MTF response curve must be extrapolated at the higher frequencies. Because a square wave pattern is used to calibrate the sensor, the measured MTF response corresponds to a square wave input modulation. To determine the AVHRR's impulse response or LSF, an equivalent sine wave MTF is required. To estimate the equivalent sine wave response ($\mathrm{MTF}(\nu)_{\mathrm{siw}}$) from the measured square wave response ($\mathrm{MTF}(\nu)_{\mathrm{sqw}}$) the following relationship was used [*Lloyd*, 1975],

$$\mathrm{MTF}(\nu)_{\mathrm{siw}} = \Pi/4\{\mathrm{MTF}(\nu)_{\mathrm{sqw}}\} \qquad \nu \geq \nu_c/5 \tag{8}$$

where ν_c is the cutoff frequency. According to Lloyd, the expression above is a good approximation for frequencies greater than about one-fifth of the cutoff frequency (i.e., the ν at which $\mathrm{MTF}(\nu)_{\mathrm{siw}} = 0.5$). Additional contraints must also be satisfied, namely, that $\mathrm{MTF}(\nu)_{\mathrm{siw}} = (\mathrm{MTF}(\nu)_{\mathrm{sqw}}$ at the lowest and the highest frequencies that define the MTF response curve. Obviously, the previous requirement must be relaxed somewhat near the minimum and maximum values of ν in order to produce a smooth, well-behaved curve.

In order to calculate LSFs for the AVHRR, information on system phase shift as well as the MTF data are required, as indicated earlier (section on linear systems). According to

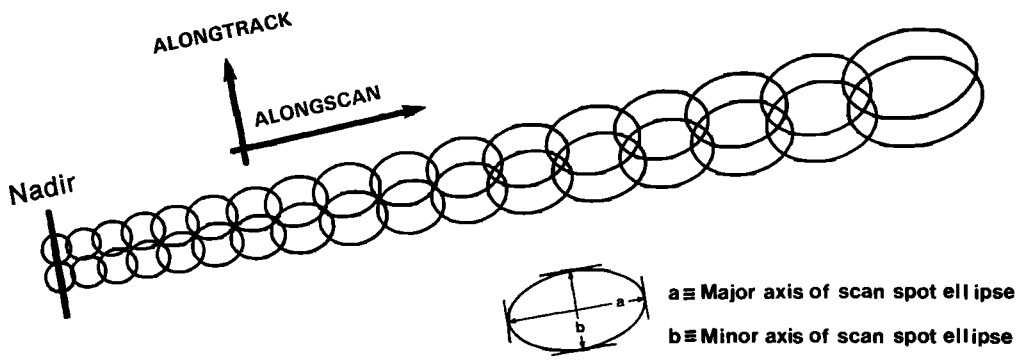

Fig. 2. Sketch of pixel geometry for the AVHRR for adjacent scan lines showing scan spot (pixel) overlap in the alongscan and alongtrack directions.

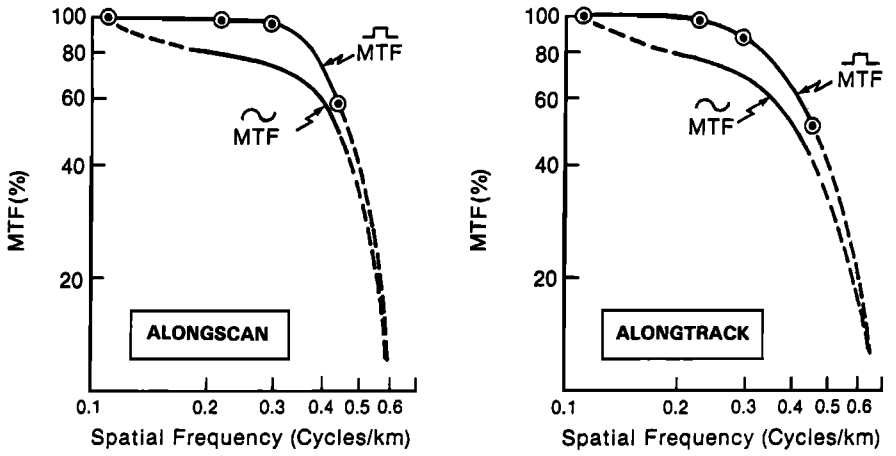

Fig. 3. AVHRR square wave and sine wave MTF response curves for band 4 (NOAA 10) for the alongscan (left panel) and the alongtrack (right panel) directions [*ITT-Aerospace*, 1976]. Circled points indicate measured values, and dashed portions indicate estimated MTF responses in those regions.

R. Koczor (personal communication, 1987), the phase shift introduced by the AVHRR occurs within the electronics and, to a first approximation, can be modeled as the phase shift that occurs in a two-pole Butterworth filter (Figure 4). This phase response applies in the alongscan direction only. As indicated by *Markham* [1984] for the MSS onboard Landsat, the corresponding filter approximation for this sensor's electronics has no effect on the alongtrack MTF (i.e., no phase shift in the alongtrack direction), and thus the same should be true for the AVHRR.

Calculating the Line Spread Functions

To estimate the line spread functions, LSF_x and LSF_y for the AVHRR, the alongscan and alongtrack MTFs are employed in accordance with the section on linear systems. These calculations are accomplished using the discrete version of the inverse Fourier transform, where the LSF at the kth point is

$$h_k = \frac{1}{N} \sum_{n=0}^{N-1} H_n e^{-2\pi i n k/N} \tag{9}$$

where h_k is the inverse Fourier transform of H_n or the LSF, H_n the system OTF at spatial frequency n, N the number of points at which the OTF is discretized, and $i = \sqrt{-1}$.

The estimated sine wave MTF response curves (Figure 3) were digitized at 32 points, equally spaced in frequency ($\Delta\nu$ = 0.025 cycles/km) from 0.0 to approximately 0.7 cycles/km. The phase response for the alongscan case (Figure 4) was digitized at the same frequencies. The actual calculations were performed using a fast Fourier transform [*Press et al.*, 1986]. The calculated LSFs for the alongscan and alongtrack directions are shown in Figures 5 and 6. Since $\Delta\nu$ and Δx are related by $\Delta\nu = 1/N\Delta x$, where ν is the spatial frequency and Δx is distance, the incremental distance along the abscissa is

$$\Delta x = 1/N\Delta\nu = 1.0/32(0.025) = 1.25 \text{ km}$$

The alongscan LSF (Figure 5) is asymmetric about the location of maximum response due to the phase shift that

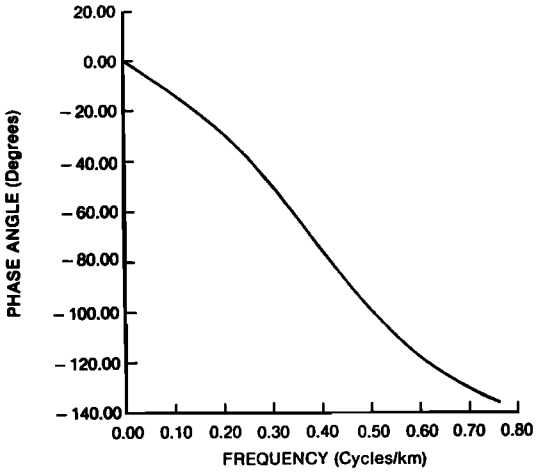

Fig. 4. Phase response for a two-pole Butterworth filter. This phase response approximates the phase response of the AVHRR (R. Koczor, personal communication, 1987).

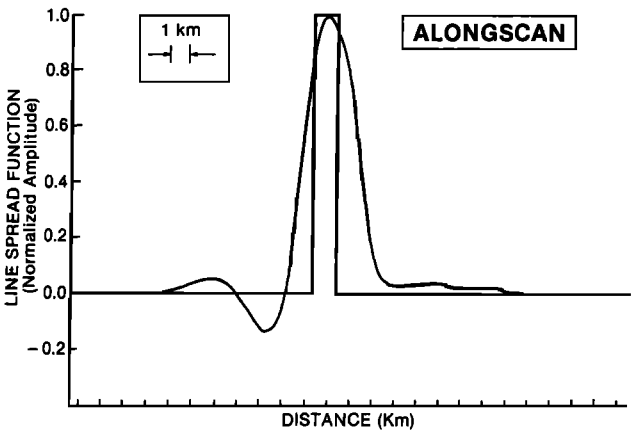

Fig. 5. The calculated LSF for the AVHRR in the alongscan direction.

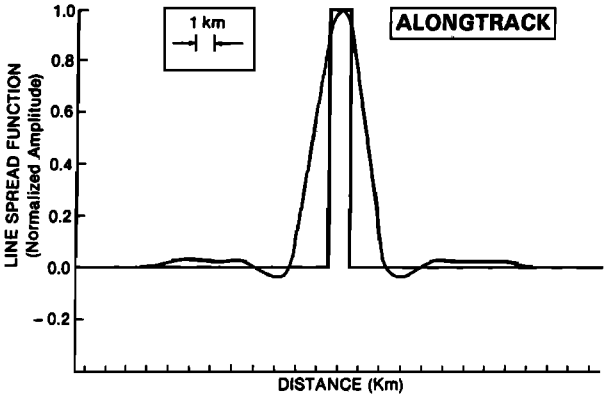

Fig. 6. The calculated LSF for the AVHRR in the alongtrack direction.

occurs in this direction. Also, its departure from an ideal LSF (i.e., rectangular) is clearly evident. In contrast, the alongtrack LSF is symmetric, although this response curve also departs significantly from an ideal response.

SENSOR SIMULATIONS

To determine the autocorrelation introduced by the AVHRR due to pixel overlap in the alongscan direction, normally distributed random sequences with zero mean and unit variance (0, 1) were produced using an IMSL Gaussian random deviate generator [*IMSL Inc.*, 1982]. Seventy sequences were generated with each containing 2048 values. (The IMSL random number generator was initially tested for randomness by calculating autocorrelation functions (ACFs) prior to the calculations described here. For 70 runs, with the same seeds used here, sequences of 512 and 2048 yielded average ACFs over lags 1–5 that ranged from 0.001 to 0.0048 for the sequence of 512, and from 0.001 to 0.0037 for the sequence of 2048. Results became sequence length dependent for sequences considerably shorter than the value used here but were not sequence length dependent for lengths of this order, or greater.) Within each sequence, values in groups of 10 were shifted to produce new sequences which were overlapped by 40%, simulating the characteristic of oversampling (in the alongscan direction) in the AVHRR. The results were then averaged within groups to produce the final overlapped series. ACFs were calculated out to lag 10 in each case. The resulting 70 ACFs were then averaged. This procedure produced a mean autocorrelation of 0.392 at lag 1, and since a value of 0.40 was the anticipated result at this lag (i.e., the expected correlation due to 40% overlap between adjacent pixels), this level of convergence was considered acceptable and thus justified the use of 70 (versus a greater number of) sequences. The autocorrelation due to overlap in the alongscan direction at lags 1–10 are listed in Table 2 and plotted in Figure 7. Autocorrelations at lags greater than 1 are probably not statistically significant (i.e., less than 0.01). Since alongscan pixel overlap for the AVHRR is less than 50%, significant correlations beyond lag 1 were not expected.

The same approach can be used to determine the correlation introduced by the AVHRR in the alongtrack direction. As was pointed out earlier, the percent of overlap between adjacent pixels in the alongtrack direction depends on the slant range (or nadir angle) between the satellite and the ground. Using the linear approximation given in the previous section, the percent of overlap between adjacent pixels in the alongtrack direction versus nadir or viewing angle from the satellite is shown in Figure 8. In this case, as before, the percent of overlap is roughly the autocorrelation to be expected at lag 1 ($\times 10^{-2}$), and since the overlap does not exceed 50% for allowable nadir angles, significant correlation beyond lag 1 due to overlap is not expected in the alongtrack direction.

Autocorrelation introduced by the AVHRR due to the system LSFs was estimated by first generating normally distributed (0, 1) random sequences of length 512 (again, results became sequence length dependent for sequences considerably shorter than this value), and then convolving the results with the corresponding LSFs. Since the LSFs

TABLE 2. Calculated Autocorrelations (Due to Overlap (Alongscan) and Alongscan and Alongtrack LSFs) and Combined Autocorrelations (for Equal Variances Due to Overlap and Alongscan and Alongtrack LSFs)

	Autocorrelation Coefficients		
		LSF	
Lag	Overlap (Alongscan)	Alongscan	Alongtrack
1	0.392	0.509	0.428
2	−0.016	0.072	0.000
3	−0.009	0.031	0.005
4	−0.006	0.037	0.030
5	−0.015	0.024	0.026
6	−0.012	0.007	0.018
7	0.001	−0.008	0.007
8	−0.005	−0.008	0.004
9	−0.010	−0.001	0.008
10	−0.010	−0.008	0.010

Lag	Combined Autocorrelation Coefficient
1	0.463
2	0.032
3	0.016
4	0.028
5	0.019

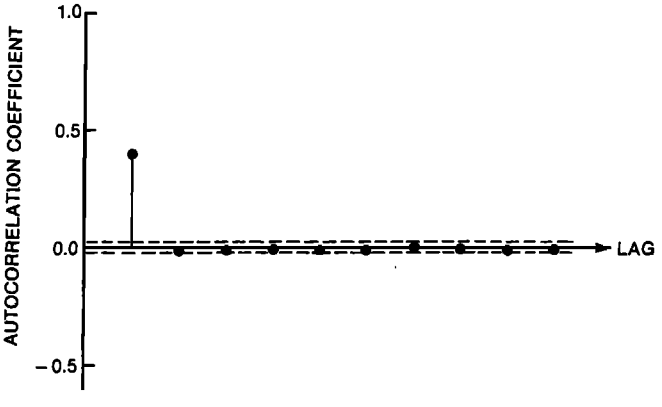

Fig. 7. Average autocorrelation function (ACF) calculated from 70 random sequences for lags 1–10 for the AVHRR due to overlap in the alongscan direction. Horizontal dashed lines indicate approximate 95% confidence limits.

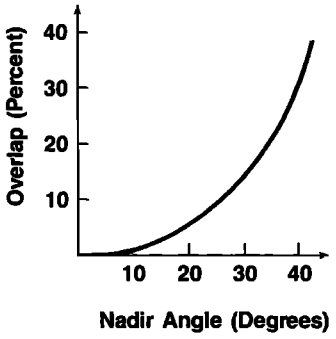

Fig. 8. Percent overlap between adjacent pixels in the alongtrack direction versus nadir angle for a satellite altitude of 870 km.

were digitized at 21 (equally spaced) points, each convolved series contained 492 values. ACFs were calculated from the convolved series and then averaged over 70 such simulated realizations. The results for the alongscan LSF (Table 2; Figure 9, upper panel) indicate that the autocorrelation at lag 1 is approximately 0.51, and at lag 2, 0.07. The autocorrelation at lag 2 may be statistically significant, a result of the asymmetry of the alongscan LSF. Simulated autocorrelations were also calculated for the alongtrack direction (Table 2; Figure 9, lower panel). The autocorrelation at lag 1 in the alongtrack direction is somewhat less than in the alongscan direction (0.43 versus 0.51). At lags greater than 1, autocorrelations in this direction are most likely not statistically significant.

Combining the Results

To determine the overall effects of sensor-induced correlation on the property of interest, the autocorrelation due to overlap (alongscan and alongtrack), and the system LSFs (alongscan and alongtrack), must be combined. If we assume that these effects arise independently, then random process theory indicates that these effects combine linearly according to [*Vanmarcke*, 1983]

$$\rho_T(\tau) = \sum_j q_j \rho_j(\tau) \tag{10}$$

where

$$q_j = \sigma_j^2 / \sum_k \sigma_k^2 \tag{11}$$

and $\rho_T(\tau)$ is the combined (T) autocorrelation at lag τ, $\rho_j(\tau)$ is the jth autocorrelation due to overlap, alongscan LSF, or alongtrack LSF at lag τ, σ_k^2 is the variance associated with the kth process, and q_j is the fractional contribution to the total variance. (Autocorrelation due to overlap and to the system LSFs may, in fact, not be completely independent. However, for the sake of expediency, we assume that any interdependence between these two effects is small.)

Representative values for the combined autocorrelations due to overlap (alongscan) and the alongscan and alongtrack LSFs at zero nadir for the AVHRR out to lag 5 are included in Table 2 and shown in Figure 10. For viewing angles off nadir, the autocorrelation due to overlap in the alongtrack direction must also be included. Estimates for this contribution were presented previously (Figure 8). These results indicate that AVHRR-induced autocorrelation may be important over the first two lags. Beyond lag 2, the autocorrelations are again most likely not statistically significant.

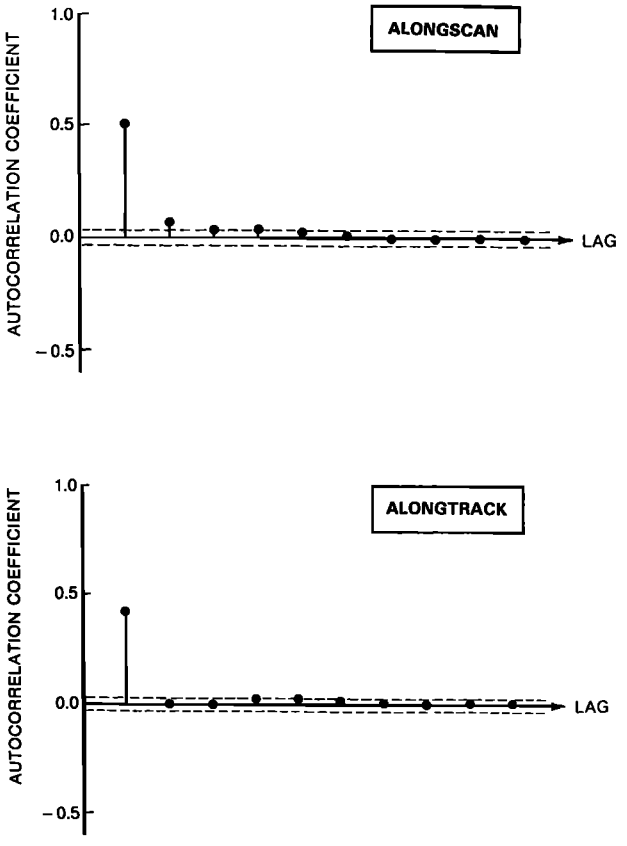

Fig. 9. Average ACF calculated from 70 random sequences for lags 1–10 for the AVHRR due to the system LSF in the alongscan (upper panel) and the alongtrack (lower panel) directions. Horizontal dashed lines indicate approximate 95% confidence limits.

It is important to note that these results depend, in part, on the values of the individual variances chosen originally (i.e., unity in each case) in performing the ACF calculations. Thus the results in the lower half of the Table 2 (and shown in Figure 10) are valid only for the case where the individual variances that contribute to the overall ACF are equal. In reality, these values are not known, and thus we can only specify the limits within which the true composite values will

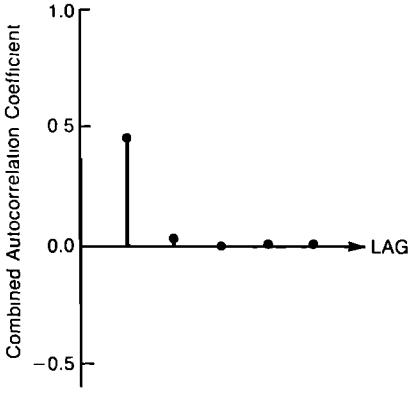

Fig. 10. Combined autocorrelation function due to overlap and the alongscan and alongtrack LSFs, at nadir, for equal variances due to overlap and alongscan and alongtrack LSFs.

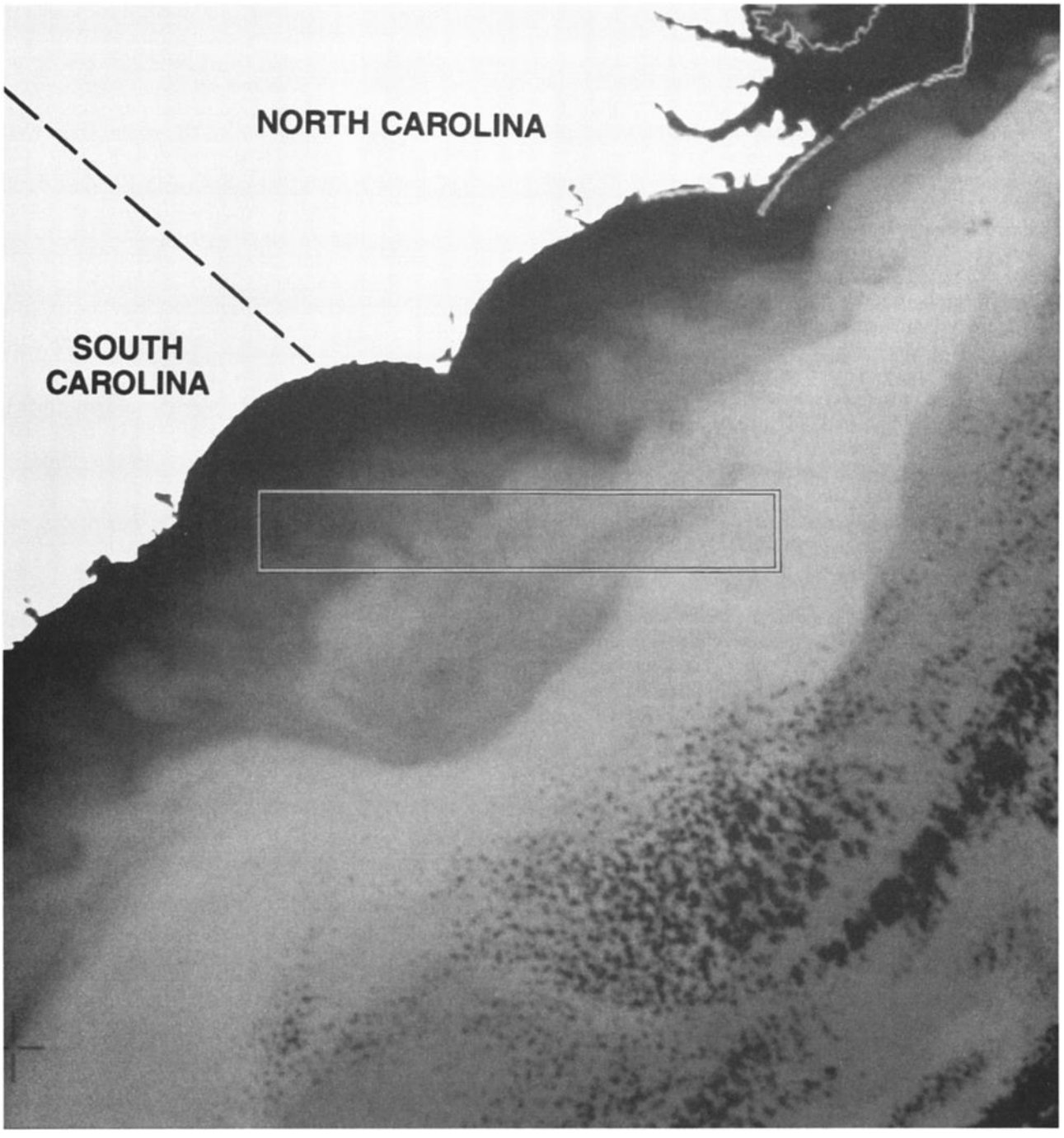

Fig. 11. AVHRR satellite image acquired on February 27, 1988, at 2030 UT over a portion of the Gulf Stream off the coasts of North and South Carolina. Darker shades indicate cooler SSTs and vice versa. The rectangle (300 km × 50 km) indicates the cloud-free area within which analyses described in the text are conducted.

lie. In principle, (10) could simply be inverted to determine the ACF of SST itself from observed AVHRR data, if each of the σ_k^2 were known. Since significant autocorrelations occur, at most, only over the first two lags, however, our results suggest an even simpler approach: subsample the raw data every third pixel in both the alongscan and alongtrack directions. Subsampling, of course, raises the specter of spatial aliasing.

APPLICATION TO OBSERVED DATA

In this section we apply the results of the previous section to observed AVHRR satellite data acquired over a cloud-free portion of the Gulf Stream on February 27, 1988, at 2030 UT. In particular, we subject the subset of satellite-derived SSTs indicated in Figure 11 to autocorrelation analysis after first detrending the data and then subsampling the residuals

every third pixel. The AVHRR data were Earth-located using standard techniques [*Brown and Evans*, 1982]. SSTs were calculated from radiances in bands 4 (10.8 μm) and 5 (12.0 μm) using the multichannel retrieval technique of *McClain et al.* [1985]. Every fifth scan line within the enclosed rectangle was selected for analysis. Each scan line contained 256 pixels.

As mentioned, the data were initially detrended. Detrending was employed to remove low wave number variability in the data caused by gradually increasing temperatures as the Gulf Stream was approached and crossed. This source of variability rendered the data nonstationary and thus, in its original form, unsuitable for autocorrelation analysis. A third-degree polynomial was fitted to each scan line using the method of least squares and then removed from the original data, yielding the residuals shown in Figure 12 (middle column). These residuals, as well as the original data, indicate the locations of Gulf Stream boundaries on its western side by the sudden increases (or changes) in SST which can be identified in certain scan lines. The residuals were subsampled every third pixel in accordance with the results of the previous section. Autocorrelation functions were then calculated from the subsampled residuals, yielding the autocorrelograms shown in Figure 12 (right-hand column).

These autocorrelograms indicate zero-crossing distances in the range of 15–25 km. First zero-crossing estimates obtained from these ACFs should be virtually unaffected by sensor-induced autocorrelation, since they occur at lag numbers considerably greater than 2. In some cases, several peaks occur in the autocorrelation plots, suggesting periodic variability in SST, with wavelengths of the order of 40 km in this region of the Gulf Stream.

DISCUSSION

From the foregoing analysis, it is apparent that the temperatures calculated from neighboring pixels will be similar at least to the extent that sensor-induced autocorrelation is important. Because of this artificially induced similarity between neighboring pixel temperatures, the magnitudes of sharp gradients and oceanic fronts over small spatial domains will be suppressed. To illustrate this effect explicitly, we simulate a sharp ocean front and then apply the smoothing functions associated with the alongscan and the alongtrack LSFs (Figure 13). The simulated front, before smoothing, has a gradient of 8°C/1 km pixel. After smoothing, in each case, small but perceptible distortions of the frontal structure occur. These distortions or discrepancies extend for about 1 pixel about the region of maximum change and result in a small but detectable reduction in the overall gradient. The magnitudes of these discrepancies are generally in the range of 1–3 counts (~0.2 to ~0.6°C). Even for full resolution imagery, these effects will be small and most likely will be detectable only in color displays. For lower resolution black and white displays, these effects will probably not be detectable.

One approach to correcting the raw data for the effect of sensor-induced autocorrelation is through the fitting of a so-called ARIMA time series model to the data [e.g., *Box and Jenkins*, 1976]. The previously calculated autocorrelation coefficients could be used to derive such an ARIMA model that could then be applied to the raw data to correct for the effect of sensor-induced autocorrelation. In addition to the ACFs, partial autocorrelation functions (PACFs) are often calculated [*Box and Jenkins*, 1976] to help determine the type and order of such models. PACFs were, in fact, calculated as a part of the present analysis (although not shown) and, together with the ACFs, suggest that a relatively simple MA(1) model is appropriate in both the alongscan and alongtrack directions. Such a model, in one spatial dimension, would have the following form (with zero mean),

$$T_x = \beta_0 z_x + \beta_1 z_{x-1} + \cdots \beta_n z_{x-n} \tag{12}$$

where the T represent temperatures at adjacent x, $x - 1$, $x - 2$, etc., locations along (or across) a scan line, the β are the moving average coefficients, and the z_x represent a white noise process.

Spatial spectra, calculated from AVHRR-derived SSTs, will also be affected by sensor-induced correlation. Since the spectrum of a first-order MA process can be expressed in one dimension as [*Chatfield*, 1984]

$$P(\nu) = \frac{1}{\pi}[1 + 2\beta \cos \nu/(1 + \beta^2)] \tag{13}$$

where $P(\nu)$ is the one-dimensional spatial spectrum at spatial frequency ν and β is a constant, it is clear that sensor-induced correlation will introduce distortion into estimates of $P(\nu)$ as well.

Preprocessing of AVHRR satellite data for SST often includes spatial averaging of adjacent pixels in blocks of four or more to reduce both the problem of cloud contamination and the volume of data. The results of spatial averaging by itself still contain the effects of sensor-induced autocorrelation. Even the preprocessing procedure employed by *Cornillon et al.* [1987], whereby they retain only the warmest pixel in each 4 × 4 pixel square, does not eliminate the problem entirely, since in some cases, adjacent pixels will be the ones retained in two adjacent squares.

In the foregoing analysis, we have only considered the effects of the sensor itself in degrading the clarity and uniqueness of the signal that represents SST from a single area on the Earth's surface. Further processing of the data, including geometric corrections and Earth location, introduces additional signal degradation. Any algorithm used to resample the original data in this regard will possess an equivalent MTF, and associated with that MTF there will be additional processing-induced effects on the correlation structure of the data.

The MTFs can also be used to provide an alternate estimate of the spatial resolution of the AVHRR. According to *Slater* [1975], such an estimate is provided by the effective instantaneous field-of-view (EIFOV) of the instrument. This measure of spatial resolution is defined as

$$\text{EIFOV}_{\text{alongscan}} = \frac{1}{2(\mu_c)} \tag{14}$$

where $\mu = \mu_c$ at MTF(μ) = 0.5 in the alongscan direction, and

$$\text{EIFOV}_{\text{alongtrack}} = \frac{1}{2(\nu_c)} \tag{15}$$

where $\nu = \nu_c$ at MTF(ν) = 0.5 in the alongtrack direction, and μ_c and ν_c are the effective system cutoff frequencies.

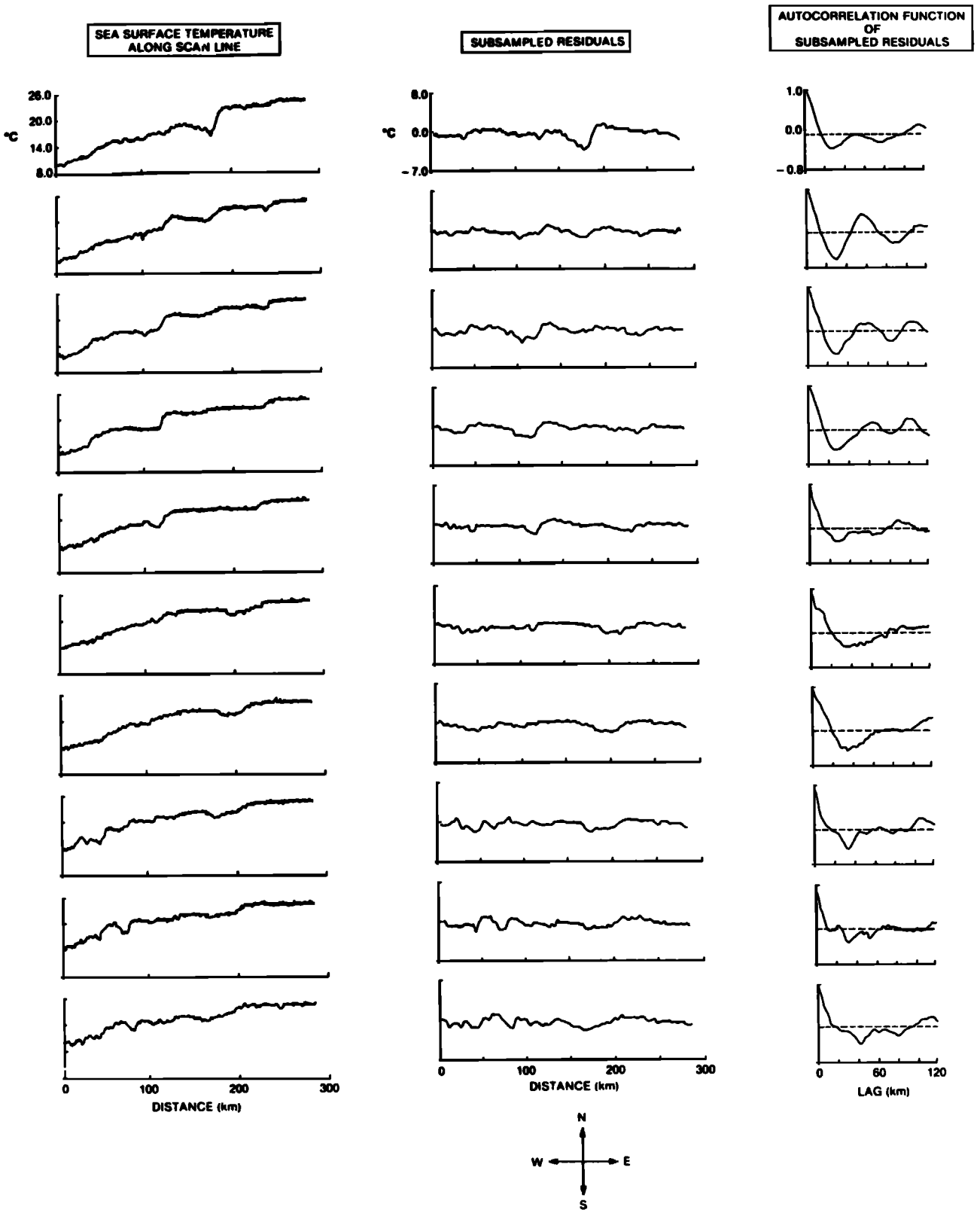

Fig. 12. The left-hand column shows SSTs derived from AVHRR satellite data along selected scan lines for the area shown in Figure 11. The center column shows the corresponding subsampled residuals (every third pixel) after third-degree least squares polynomials were removed from the data. The right-hand column shows the corresponding subsampled autocorrelation functions for each scan line.

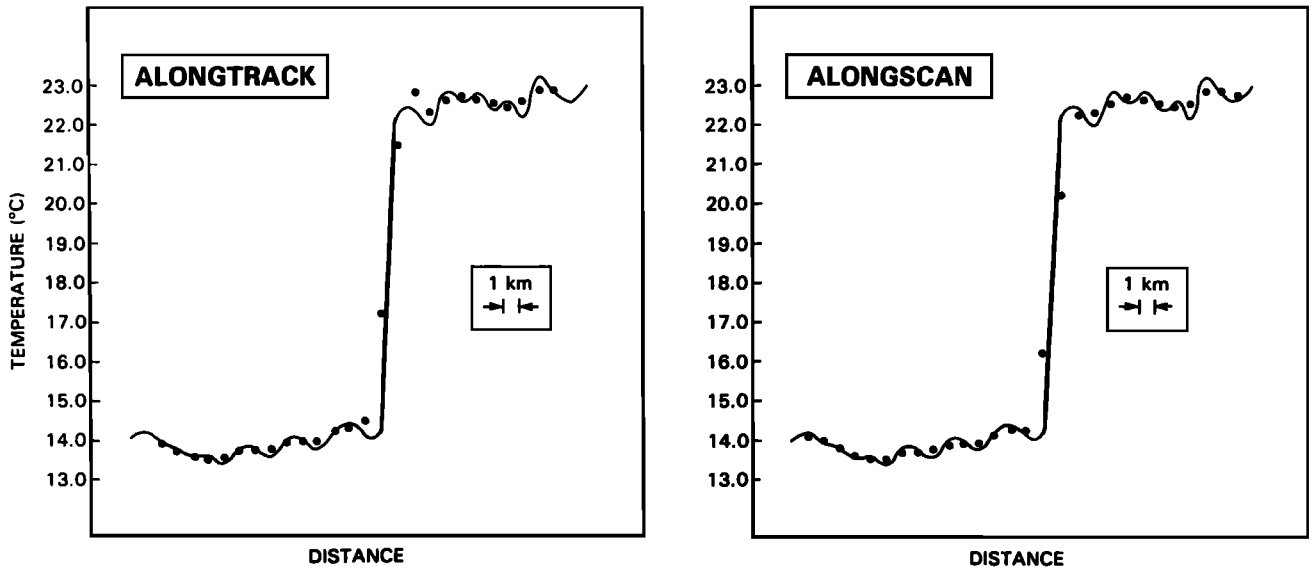

Fig. 13. Smoothing across a simulated ocean front due to alongscan (right panel) and alongtrack (left panel) LSFs. Solid lines indicate the simulated front before smoothing, and the dots, the simulated front after smoothing (i.e., as the AVHRR "sees" it).

When the appropriate values are taken from Figure 3, (14) and (15) yield EIFOVs of approximately 1.20 km in the alongscan direction and approximately 1.28 km in the alongtrack direction. These results indicate (1) that the AVHRR pixel geometry is asymmetric and (2) that the effective spatial resolution of the instrument, as defined above, is somewhat lower than the nominal value of 1.1 km (at nadir). These results parallel those of *Park et al.* [1984], who found EIFOVs for the MSS aboard Landsat to be significantly larger than the commonly accepted values(s) for the spatial resolution of that instrument. Due to an effective lower spatial resolution for the AVHRR, previous estimates of gradient strength across oceanic fronts, for example, have probably been overestimated (by ~10%).

Finally, we consider the accuracy of the calculations performed in the analysis above. First, the MTF data used here are representative of the AVHRR only to the extent that the particular instrument on the NOAA 10 spacecraft is representative of the other radiometers that have been, or will be, flown in this series. The accuracy of the calculations themselves can be questioned on several grounds. First, MTF data are only available at four discrete spatial frequencies and in no case span the entire frequency range of interest. Thus the MTF data must be extrapolated at higher frequencies to provide a complete response function. The errors that might be expected in this extrapolation have not been estimated. Also, the error introduced by estimating a sine wave approximation to the square wave MTF provided by the manufacturer is not known. As indicated, it has been assumed throughout that the effect of sensor-induced autocorrelation due to pixel overlap is independent of that due to the system LSFs. Any interdependence of these effects will most likely detract from the accuracy of the results. On the positive side, however, although these errors may affect the autocorrelations that were calculated, and could influence the EIFOV results, the overall results concerning the number of pixels over which sensor-induced autocorrelation is significant, should be relatively insensitive to such errors.

CONCLUSIONS

AVHRR satellite data are significantly correlated at the lowest spatial lags in both the alongscan and alongtrack directions due to (1) overlap of adjacent pixels and (2) nonideal LSFs. Simulated autocorrelations in the alongscan direction are approximately 0.4 due to overlap and approximately 0.51 due to the LSF at lag 1, small but possibly significant at lag 2, and not significant beyond lag 2. Autocorrelation due to pixel overlap is different in the alongtrack direction because the percent of overlap is not constant but increases with increasing satellite scan angle. Autocorrelation due to nonideal LSFs is slightly greater in the alongscan direction due, in part, to a nonzero phase shift that occurs in the AVHRR electronics.

To avoid the problem of sensor-induced autocorrelation, the raw data should be subsampled every third pixel. To avoid sensor-induced autocorrelation with no loss of data, a time series ARIMA model could be employed with coefficients derived from the previously calculated autocorrelations. Spatial averaging of adjacent pixels does not eliminate the problem of sensor-induced autocorrelation in AVHRR satellite data. The EIFOV of the AVHRR (NOAA 10) indicates that the spatial resolution of this instrument is somewhat less (~1.25 km) than the nominal value of 1.1 km (at nadir). Correlation length scales for SST for AVHRR satellite data subsampled in accordance with the results of this study are consistently in the neighborhood of 20 km over one portion of the Gulf Stream. Sensor-induced correlation results in a small but detectable suppression of the gradients associated with sharp oceanic fronts. That the effective spatial resolution of the AVHRR is lower than the nominal value which has been previously assumed, leads to overestimates of gradient strength of the order of 10%.

The accuracy of the simulated autocorrelations presented for the AVHRR is, in part, limited by (1) an incomplete specification of the MTF response function and (2) the necessity of estimating a sine wave MTF from the square

wave MTF data which are available. It is recommended that additional calculations be performed to determine the sensitivity of the results presented here to the sources of error indicated above.

Finally, sensor-induced autocorrelation can also be expected to contribute to interpixel correlations for other spaceborne radiometers such as the MSS (on Landsat), the CZCS (on Nimbus 7), and the OLS (on the Defense Meteorological Satellite Program (DMSP)) satellites. The approach used in this study should be useful in quantifying sensor-induced correlation for these sensors as well.

Acknowledgments. The author thanks H. Jean Thiebaux (NOAA/NWS) and Michael P. Weinreb (NOAA/NESDIS) for reviews of an early version of this paper. Many helpful comments by Richard G. Craig (Kent State University) are also greatly appreciated. The author wishes to express his gratitude to Richard Legeckis (NOAA/NESDIS) for providing the AVHRR satellite data used in this study. OPC contribution 25.

REFERENCES

Box, G. P., and G. M. Jenkins, *Time Series Analysis: Forecasting and Control*, Holden-Day, San Francisco, Calif., 1976.

Brown, O. B., and R. Evans, Visible and infrared satellite remote sensing—A status report, *Nav. Res. Rev.*, *31*, 7–25, 1982.

Chatfield, C., *The Analysis of Time Series: An Introduction*, Chapman and Hall, London, 1984.

Cornillon, P., C. Gilman, L. Stramma, O. Brown, R. Evans, and J. Brown, Processing and analysis of large volumes of satellite-derived thermal infrared data, *J. Geophys. Res.*, *92*, 12,993–13,002, 1987.

Craig, R. G., Autocorrelation in LANDSAT data, Proceedings, 13th International Symposium on Remote Sensing of the Environment, pp. 1517–1524, Environ. Res. Inst. of Mich., Ann Arbor, 1979.

Craig, R. G., Precision in the evaluation of LANDSAT autocorrelation: The terrain effect, Proceedings, 15th International Symposium on Remote Sensing of the Environment, pp. 1305–1313, Environ. Res. Inst. of Mich., Ann Arbor, 1981.

Craig, R. G., Evaluation of terrain complexity by autocorrelation, final report, contract NAG5-165, Natl. Aeronaut. and Space Admin., Washington, D. C., 1982.

Craig, R. G., The spatial structure of terrain: A process signal in satellite digital images, 1984 Proceedings of PECORA 9 Spatial Information Techniques for Remote Sensing Today and Tomorrow, pp. 51–54, IEEE, New York, 1984.

Craig, R. G., and M. L. Labovitz, Sources of variation in LANDSAT autocorrelation, Proceedings, 14th International Symposium on Remote Sensing of the Environment, pp. 1755–1767, 1980.

Gaskill, J. D., *Linear Systems, Fourier Transforms, and Optics*, John Wiley, New York, 1978.

Goodman, J. W., *Introduction to Fourier Optics*, McGraw-Hill, New York, 1968.

IMSL, Inc., *IMSL Library Reference Manual*, ed. 8, vol. 2, Houston, Texas, 1982.

ITT-Aerospace, Advanced very high resolution radiometer, technical description, revision D, contract NAS 5-22497, Opt. Div., Ft. Wayne, Indiana, 1976.

Lloyd, J. M., *Thermal Imaging Systems*, Plenum, New York, 1975.

Markham, B. L., Characterization of the LANDSAT sensor's spatial responses, *NASA Tech. Memo.*, *86130*, 1–68, 1984.

Markham, B. L., The LANDSAT sensor's spatial responses, *IEEE Trans. Geosci. Remote Sens.*, *GE-23*, 864–875, 1985.

McClain, E. P., W. G. Pichel, and C. C. Walton, Comparative performance of AVHRR-based multichannel sea surface temperatures, *J. Geophys. Res.*, *90*, 11,587–11,601, 1985.

Park, S. K., R. Schowengerdt, and M. Kaczynski, Modulation-transfer-function analysis for sampled image systems, *Appl. Opt.*, *23*, 2572–2582, 1984.

Press, W. H., B. P. Flannery, S. A. Teukolsky, and W. T. Vetterling, *Numerical Recipes, The Art of Scientific Computing*, Cambridge University Press, New York, 1986.

Richards, J. A., *Remote Sensing Digital Image Analysis: An Introduction*, Springer-Verlag, New York, 1986.

Schwalb, A., The TIROS-N/NOAA A-G satellite series, *NOAA Tech. Memo*, *TM NESS 95*, 75 pp., 1978.

Slater, P. N., Use of MTF specification and first-order design of electro-optical and photographic imaging and radiometric systems, *Opt. Acta*, *22*, 277–290, 1975.

Tubbs, J. D., and W. A. Coberly, Spatial correlation and its effect upon classification results in LANDSAT, Proceedings, 12th International Symposium on Remote Sensing of the Environment, Environ. Res. Inst. of Mich., Ann Arbor, 1978.

Vanmarcke, E., *Random Fields: Analysis and Synthesis*, MIT Press, Cambridge, Mass., 1983.

L. C. Breaker, NOAA/NWS, National Meteorological Center, WMB, W/NMC 21, Room 206, Washington, DC 20233.

(Received October 20, 1988;
revised May 20, 1989;
accepted May 20, 1989.)